ISIJ International, Vol. 45 (2005), No. 3, pp. 325–330

# Comparison between Standard and Renormalization Group $k$–$\varepsilon$ Models in Numerical Simulation of Swirling Flow Tundish

Qinfu HOU and Zongshu ZOU[1)]

Doctoral candidate, College of Materials and Metallurgy, Northeastern University, 110004 Shenyang, P. R. China. E-mail: hqf780826@126.com 1) College of Materials and Metallurgy, Northeastern University, 110004 Shenyang, P. R. China. E-mail: zouzs@mail.neu.edu.cn

(*Received on September 30, 2004; accepted in final form on December 20, 2004*)

Because of the introduction of a cylindrical swirling chamber into a neotype tundish, the Swirling Flow Tundish (SFT), the numerical simulation becomes difficult for this kind of tundish by the standard two-equation $k$–$\varepsilon$ turbulence model. So another kind of $k$–$\varepsilon$ turbulence model, the Renormalization Group (RNG) $k$–$\varepsilon$ turbulence model derived from the theory of renormalization group, was adopted and compared with the standard one. Both of these two kinds of turbulence models were used to simulate the flow patterns in SFT on staggered grid systems based on Finite Volume Method (FVM) with SIMPLER algorithm for steady 3D and incompressible Newtonian turbulent flows. The comparison of simulation results from these two models shows that the RNG $k$–$\varepsilon$ turbulence model for SFT leads quicker convergence than the standard one. Unsymmetrical flow patterns were obtained and the grid independence of this mathematical model for SFT was also discussed. The theoretical analyses of forces on particle, turbulent kinetic energy distribution and lower flow velocity behind dam and weir show that there will be a good effect for non-metal inclusion aggregation and separation with the swirling chamber.

KEY WORDS: swirling flow tundish; renormalization group; standard $k$–$\varepsilon$ turbulence model; numerical simulation.

## 1. Introduction

Flows in tundishes have been intensively studied through numerical simulations by many researchers in the past several decades. In these studies, the standard $k$–$\varepsilon$ turbulence model with two-equation was commonly adopted (He and Sahai,[1)] LEE and KOO,[2)] JHA,[3)] Palafox-Ramos[4)] and Fan[5)]). Nine kinds of turbulence models have been used for prediction of fluid mixing in tundish by JHA,[6)] including the standard two-equation $k$–$\varepsilon$ turbulence model and the Renormalization Group (RNG) turbulence model. It's evident that the RNG turbulence model is seldom used by researchers in the simulation of metallurgical processes. Since it was first put forward by Yakhot,[7,8)] however, the RNG turbulence model has been used widely (Analytis,[9)] Ponser,[10)] MING.,[11)] Sierra-Espinosa,[12)] Matthews,[13)] XIA[14)] and MOMPEAN[15)]) in other areas for numerical simulations. During the tundish process, many kinds of Turbulence Inhibiting Pad (TIP)[16)] or Flow Control Device (FCD)[5)] were used to smoothen the flow and improve the removal of inclusions from molten steel. Among which the Centrifugal Flow Tundish (CFT) developed by Kawasaki Steel[17)] has shown the greatest potential of inclusion removal. External rotating electromagnetic field, however, must be used in a CFT. In a Swirling Flow Tundish (SFT),[18)] a cylindrical swirling chamber is installed in a conventional tundish to form a rotational flow in the chamber by introducing the liquid strand into the chamber bottom tangentially, *i.e.* to transform the translational energy of the liquid strand into rotational one. In order to simplify the numerical simulation processes, and since the results can be accepted with small difference to inclined walls,[1)] vertical walls are adopted for physical prototype with inclined wall. The structure of the simplified swirling flow tundish for numerical simulation is shown in **Fig. 1**, with swirling chamber, weir and dam. Because of the introduction of the swirling chamber, some problems arise during numerical simulation processes of swirling flow tundish such as strong curvature of flows in swirling chamber and greater difference between flow velocities in the chamber and behind the dam and weir than other types of tundish system with only TIP, weir and dam. The fierce turbulence in the swirling chamber can cause great dissipation of mechanical energy and, at the same time, enhance the collision

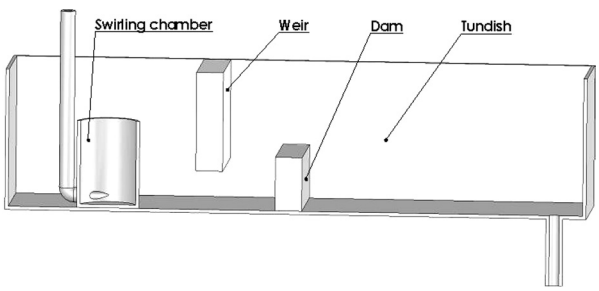


**Fig. 1.** Schematic of simplified swirling flow tundish for numerical simulation.

and coalescence of inclusions from small particles to big ones. Then, the liquid velocities behind the weir and dam will be lower. The most important effect of these problems is that the convergence results of numerical simulation are difficult to be obtained with standard $k$–$\varepsilon$ turbulence model.

In this paper, the Renormalization Group (RNG) $k$–$\varepsilon$ turbulence model is used to resolve this problem in tundish flow simulation.

## 2. Turbulence Models

The standard $k$–$\varepsilon$ turbulence model is a semi-empirical model based on the model transport equations for the turbulence kinetic energy and its dissipation rate. The model dependent constants are determined empirically and the standard values for these constants are suggested by Launder and Spalding.[19] The model transport equation for $k$ is derived from the exact equation, while the model transport equation for $\varepsilon$ was obtained by physical reasoning and bears little resemblance to its mathematically exact counterpart. In the derivation of the $k$–$\varepsilon$ model, it was assumed that the flow is fully turbulent, and the effect of molecular viscosity is negligible. The standard $k$–$\varepsilon$ model is, therefore, only valid for fully turbulent flows with high Reynolds number. Although the standard $k$–$\varepsilon$ turbulence model has gained success in many cases,[1–6] it can over-predict the level of turbulence in more complex geometries[9] for example swirling flow tundish with dam and weir.

The RNG-based $k$–$\varepsilon$ turbulence model is derived from the instantaneous Navier–Stokes equations, using a mathematical technique called 'renormalization group' (RNG). The analytical derivation results in a model with constants different from those in the standard $k$–$\varepsilon$ model, and additional terms and functions in the transport equations for k and $\varepsilon$. The constants are determined from first principles and the standard values for these constants are suggested by Yakhot and Orszag.[7] The RNG turbulence model is equally valid for both low and high Reynolds number flows. For this feature, the RNG model is more suitable for swirling flow tundish with flows of different Reynolds numbers.

### 2.1. Standard $k$–$\varepsilon$ Turbulence Model

For steady 3D Newtonian and incompressible turbulence flow, the mathematical model of standard $k$–$\varepsilon$ turbulence model can be represented as follows.

Equation of continuity

$$\frac{\partial u_i}{\partial x_i} = 0 \quad \text{.....(1)}$$

Momentum balance equation

$$\rho \frac{\partial (u_i u_j)}{\partial x_j} = -\frac{\partial p}{\partial x_i} + \frac{\partial}{\partial x_j}\left[\mu_{\text{eff}}\left\{\frac{\partial u_i}{\partial x_j} + \frac{\partial u_j}{\partial x_i}\right\}\right] \text{....(2)}$$

Turbulent kinetic energy

$$\rho \frac{\partial}{\partial x_j}\left(u_j k - \frac{\mu_{\text{eff}}}{\sigma_k} \times \frac{\partial k}{\partial x_j}\right) = G - \rho\varepsilon \text{ .....(3)}$$

**Table 1.** Constants of turbulence models used in numerical simulation.

| Model | Standard | | | | | RNG | | |
|---|---|---|---|---|---|---|---|---|
| Constants | $C_1$ | $C_2$ | $C_\mu$ | $\sigma_k$ | $\sigma_\varepsilon$ | $C_\mu$ | $C_1$ | $C_2$ |
| | 1.44 | 1.92 | 0.09 | 1.00 | 1.30 | 0.0845 | 1.42 | 1.68 |

**Table 2.** Dimensions of numerical simulation model.

| Dimensions | Length | Width | Height | L1 | L2 | L3 |
|---|---|---|---|---|---|---|
| Values, mm | 1740 | 650 | 420 | 650 | 950 | 95 |

Dissipation rate of $k$

$$\rho \frac{\partial (u_j \varepsilon)}{\partial x_j} = \frac{\partial}{\partial x_j}\left(\frac{\mu_{\text{eff}}}{\sigma_\varepsilon} \times \frac{\partial \varepsilon}{\partial x_j}\right) + \frac{(C_1 G\varepsilon - C_2 \rho \varepsilon^2)}{k} \text{ ....(4)}$$

where,

$$G = \mu_t \frac{\partial u_j}{\partial x_i}\left(\frac{\partial u_j}{\partial x_i} + \frac{\partial u_i}{\partial x_j}\right) \text{.....(5)}$$

The effective viscosity is,

$$\mu_{\text{eff}} = \mu + \mu_t = \mu + \rho C_\mu \frac{k^2}{\varepsilon} \text{ .....(6)}$$

The recommended constants by Launder and Spalding[19] are listed in **Table 1**.

### 2.2. Renormalization Group (RNG) $k$–$\varepsilon$ Turbulence Model

For steady 3D Newtonian and incompressible turbulence flow, the mathematical model of RNG $k$–$\varepsilon$ turbulence model can be represented as the same as the standard $k$–$\varepsilon$ turbulence model except for the effective viscosity.[12]

The effective viscosity is calculated by

$$\mu_{\text{eff}} = \mu\left(1 + \sqrt{\frac{C_\mu}{\mu}}\frac{k}{\sqrt{\varepsilon}}\right)^2 \text{.....(7)}$$

The constants for RNG turbulence model are also given in Table 1.

## 3. Grid System

The dimensions of the simplified tundish with vertical walls are given in **Table 2**. L1 is the distance between the left wall and weir and L2 is the distance between the dam and the right wall. L3 is the distance between the outlet and the nearest wall. The grid system for the swirling flow tundish with a swirling chamber (Height: 260 mm, Diameter: 200 mm) is shown in **Fig. 2**, which are orthogonal grid. In Fig. 2, the density of grid is also shown where the dense grids are double of the sparse ones. The sparse grids are 92×38×25 while the dense are 184×76×50. It's not a uniform one with more nodes at the inlet, outlet, dam and weir.

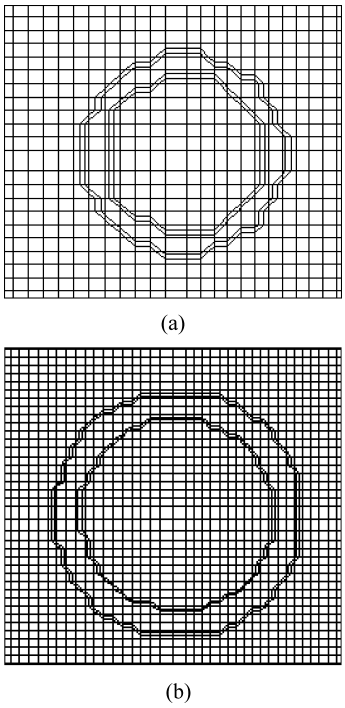

**Fig. 2.** Grid systems of *xy*-plane (section A). (a) Sparse grid, (b) dense grid.

## 4. Boundary Conditions

Near the wall boundary, the log-law-based wall function was used, which assumes the settled near-wall node to lie in the fully turbulent region with a sufficient grid distant to the wall. The walls were set to non-slip condition.

The diameters of the inlet and outlet of the physical model are 30 mm. In order to ensure the mass balance condition, however, the areas of the inlet and outlet were re-calculated according to the grid arrangement for setting the corresponding velocities. The inlet velocity was set as 1.0 m/s according to the physical prototype. The values for $k$ and $\varepsilon$ at the inlet were calculated with the following empirical equations.[20)]

$$k_{in}=0.001U_{in}^2 \quad \text{.....(8)}$$

$$\varepsilon_{in}=2k_{in}^{3/2}/D_{in} \quad \text{.....(9)}$$

In order to distinguish the outlet, inlet, swirling chamber, dam and weir, different material IDs of cell in specific areas have been assigned respectively. The residual for the convergence criterion is $10^{-4}$.

## 5. Results and Discussion

The governing equations are solved based on FVM by SIMPLER algorithm on staggered grids. The usual grid-dependent tests were also performed. The results will be discussed in the following sections. In order to show the differences in flows clearly, the whole flow field is divided into two sections: A for the part before weir and B for the part behind weir. The arrow length represents the magnitude of the local velocity vector relative to the scales shown on the top of each figure.

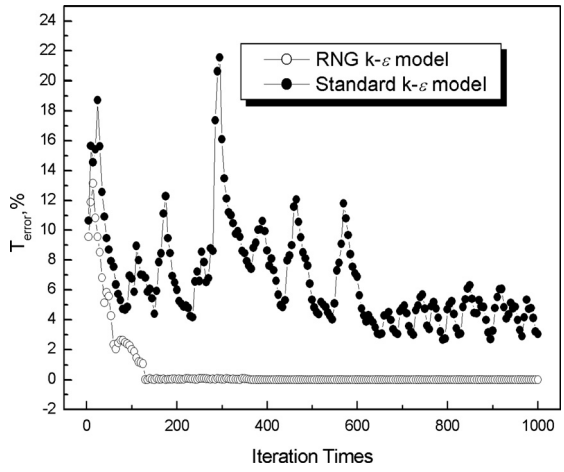


**Fig. 3.** Variation of total error with iteration.

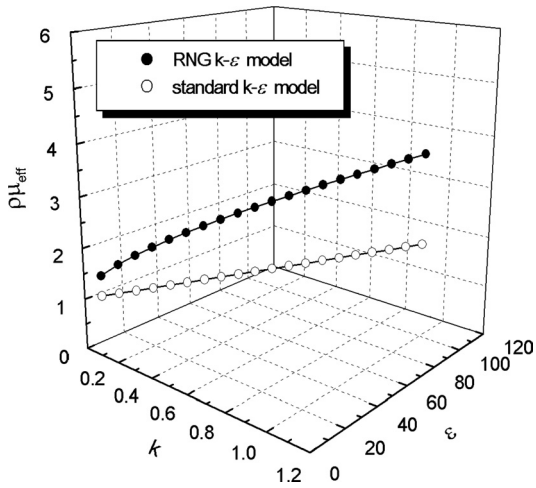


**Fig. 4.** Comparison of effective viscosity between standard and RNG $k$–$\varepsilon$ models.

### 5.1. Comparison of Convergence between the Two Turbulence Models

The total errors for each iteration step with these two different turbulence models are shown in **Fig. 3**. It's clear that convergent result can be obtained more quickly by RNG $k$–$\varepsilon$ turbulence model (Iterations: 800) than by standard $k$–$\varepsilon$ turbulence model. The convergent result can hardly be obtained with standard $k$–$\varepsilon$ turbulence model even after several thousands iterations. When the iterations are more than 600, in fact, oscillation of total errors happens within a small domain (less than 4%).

### 5.2. Comparison of Effective Viscosity between the Two Turbulence Models

Since the key difference between the two models was the equation for the effective viscosity, Eq. (6) for standard $k$–$\varepsilon$ turbulence while Eq. (7) for RNG $k$–$\varepsilon$ turbulence model, comparison was performed by calculating the effective viscosity under the real calculated domain of turbulence kinetic energy (0–100) and its dissipation rate (0–1). The result is shown in **Fig. 4** with multiplied effective viscosity by density of fluid ($\rho$). Small differences of the effective viscosity's values and their variation trends between these two types of turbulence models were observed under different

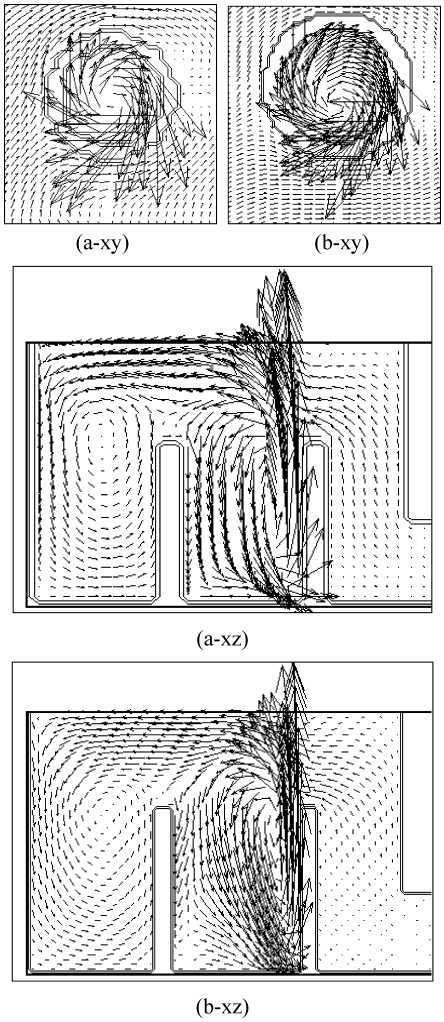


**Fig. 5.** Flow patterns (*xy*-plane, $z/H=0.38$ and *xz*-plane, $y/H=0.50$). (a) Sparse grid, (b) dense grid.

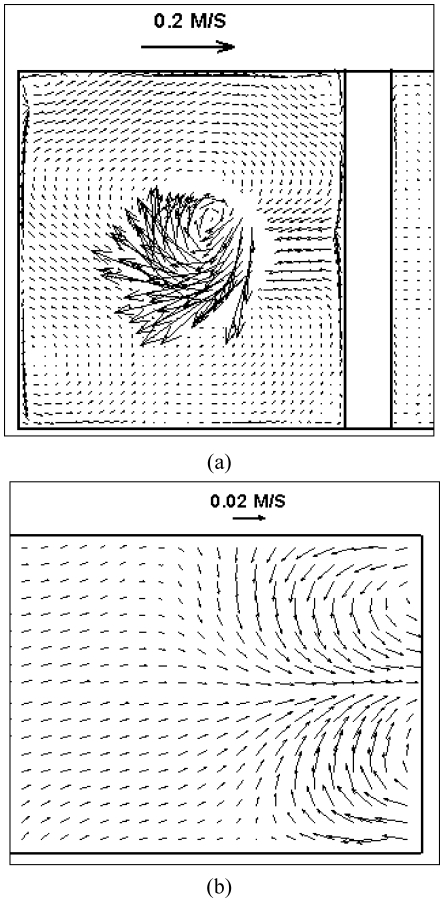


**Fig. 6.** Asymmetry of flow pattern (*xy*-plane, $z/H=0.64$). (a) Section A, (b) section B.

turbulence kinetic energy and its dissipation rate.

It's evident (shown in Fig. 1) that the RNG $k$–$\varepsilon$ turbulence model is better for getting a convergent result than the standard $k$–$\varepsilon$ turbulence model. The constants values for turbulence models are different (shown in Table 1) while those of RNG were obtained by theoretical analysis. Conclusion can thus be drawn that it's the difference of constants values and equations for effective viscosity calculation that cause the difference in convergence. The RNG $k$–$\varepsilon$ turbulence model is more suitable for swirling flow tundish than the standard $k$–$\varepsilon$ turbulence model.

### 5.3. Demonstration of Grid Independence

To verify that the mathematical model employed in the present study is grid independent, the flow patterns for the tundish with sparse and dense grids (shown in Fig. 2) were simulated, and the results are shown in **Fig. 5**. There is little difference between the flow patterns of these two kinds of grids except for the velocities behind the weir and dam. The velocities behind the weir and dam are so small that these differences are not significant. So grid independence was confirmed.

### 5.4. Asymmetry of Flow Patterns

Because of the introduction of swirling chamber and the special inlet position at a tangential direction (shown in Fig. 1), the flow patters in swirling flow tundish are sure to be unsymmetrical, which can be clearly seen in Fig. 5 and **Fig. 6**. Unsymmetrical flow patterns are evident before the weir. The flow patterns are still unsymmetrical even near the outlet (shown in Fig. 6).

Unsymmetrical flow patters have been reported by G. Solorio-Díaz[20] and neglected by many researchers who use symmetrical condition to save the time of calculation. But G. Solorio-Díaz considered that the asymmetry of flow patterns is mainly caused by the feature of turbulence fluctuation. But here in a SFT, the asymmetry of flow pattern is caused mostly by the swirling flow out of the swirling chamber. The amplitude and extent of the flow asymmetry are much greater than those in conventional tundishes.

### 5.5. Analyses of Non-metal Inclusion Separation

In the swirling flow tundish, the improvement on inclusion separation and removal can be expected from two parts mainly: (a) inclusions concentrate into the center of the swirling chamber under the centripetal force and then collide and aggregate into big ones, (b) inclusions float up onto the metal/slag interface in the very slow velocity field behind dam and weir.

Since the density of inclusion ($4\,000\,kg/m^3$) is smaller than that of molten steel ($7\,000\,kg/m^3$), the inclusions in the swirling chamber will concentrate into the center area under the centripetal force. The forces on a particle in the swirling flow chamber are shown in **Fig. 7**. Since the three-

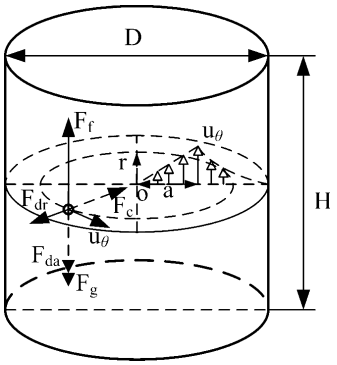


**Fig. 7.** Schematic of forces on inclusion particle and radial velocity distribution.

dimensional turbulence flow is very complicate in the swirling chamber, the forces acting on inclusion particles are hard to calculate precisely. Here, for simplification, only a simple model for this phenomenon is given. The force balance in radial direction is given by following equation where the movement of the particle is assumed in stokes regime ($Re_p<1$). The drag force on particle in stokes regime can be expressed as $F_d=3\pi\mu u_r d$.

$$\frac{\pi}{6}d^3\rho_s\frac{du_r}{dt}=\frac{\pi}{6}d^3(\rho-\rho_s)\omega^2(R_0-r)-3\pi\mu d(u_r-u_{r0}) \quad \text{.....(10)}$$

where

$$\frac{du_r}{dt}=\frac{d^2r}{dt^2},\quad u_r=\frac{dr}{dt}$$

By modifying the velocity distribution of Rankine[21] for finite domain ($R=D/2$), the distribution of velocity in circumferential direction can be given by the following equation.

$$u_r=\begin{cases}\omega r & r\le a\\ \omega a^2\left(\dfrac{1}{r}-\dfrac{4}{D(D-2a)}r+\dfrac{4a}{D(D-2a)}\right) & a<r\le D/2\end{cases} \quad \text{.....(11)}$$

The schematic distribution of circumferential velocity is shown in Fig. 7 where only the variation trend is roughly illustrated. In fact, in this small cylinder chamber, the boundary layer is so thin that radius of the central vortex is nearly equal to radius of the swirling chamber. Consequently, linear velocity distribution can be used to analyse the forces on inclusions. It can reasonably be assumed that the initial radial velocity of the inclusion is equal to zero. Then the movement of an inclusion particle toward the center can be analyzed by solving Eq. (10). The general solution gives

$$r=R_0+\frac{R_0}{r_1-r_2}(r_2e^{r_1t}-r_1e^{r_2t}) \quad \text{.....(12)}$$

where $r_1$ and $r_2$ are the roots of Eq. (10)'s character equation and are expressed as

$$r_1=(-F_D+\sqrt{F_D^2-4M_pF_c})/(2M_p)$$
$$r_2=(-F_D-\sqrt{F_D^2-4M_pF_c})/(2M_p)$$

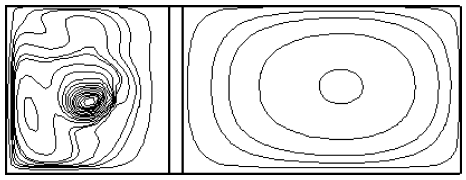

**Fig. 8.** Predicted velocity contours on *xy*-plane at $z/H=0.80$.

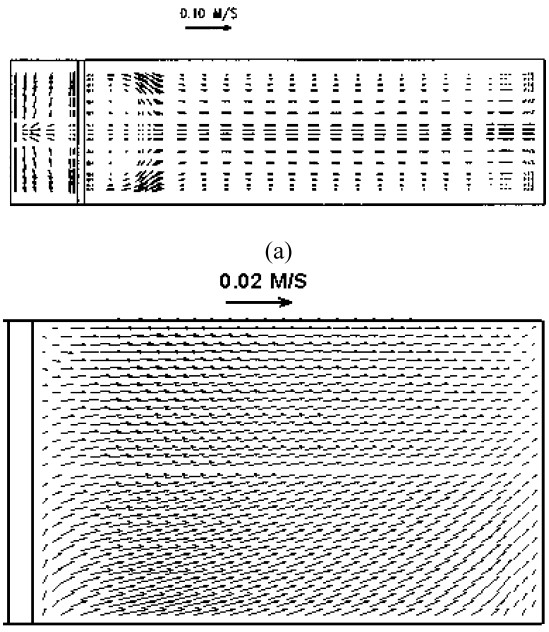


**Fig. 9.** Predicted velocity vectors at *xy*-plane. (a) $z/H=0.95$ (Ref. 22)), (b) section B at $z/H=0.80$.

where, $F_D=3\pi\mu u_r$, $M_p=\pi d^3\rho_s/6$, $F_c=\pi d^3(\rho-\rho_s)/6$.

Equation (12) shows that there is significant immigration of an inclusion toward the center of the swirling chamber, especially for inclusions of big size.

In order to show the improved flow for inclusion aggregation, a contour plot of turbulent kinetic energy is given in **Fig. 8**. It shows that turbulent kinetic energy is confined in entry zone.

Behind the dam and the weir, the flow of the swirling flow tundish is more stable than those of other kind of tundishes with different flow control device (**Fig. 9**). Consequently, more inclusions can float out and the metal/slag interface is calmer to prevent slag entrapment into steel.

## 6. Conclusions

The flow patterns of a neotype tundish, swirling flow tundish with swirling chamber, have been studied by two types of turbulence models (standard and RNG $k$–$\varepsilon$ turbulence models). The main conclusions derived from this study are as follows.

(1) The numerical simulation results show that the RNG $k$–$\varepsilon$ turbulence model is more suitable for this neotype tundish and can get convergent results more easily than the standard $k$–$\varepsilon$ turbulence model for strong curvature flows and flows with different Reynolds numbers in different areas.

(2) The grid independent feature of this numerical model (RNG $k$–$\varepsilon$ turbulence model) was verified by two kinds of grids with different node densities.

(3) The unsymmetrical flow patterns of swirling flow tundish are mainly caused by the swirling flow out of the swirling chamber, partly because of turbulence fluctuation.

(4) Under the centripetal force field, the inclusion can move to the center of swirling chamber and aggregate into a big one. The calm metal/slag interface and turbulent kinetic energy confinement in entry zone are favorable for inclusions to aggregation and floatation.

Nomenclature:

$k$: Turbulent kinetic energy
$k_{in}$: Turbulent kinetic energy at inlet
$u_i$: Mean velocity in the $x_i$-direction
$u_{in}$: Mean velocity at inlet
$u_\theta$: Circumferential velocity in swirling chamber
$u_r$: Radial velocity in swirling chamber
$F_{rd}$: Drag force in radial direction
$F_{ad}$: Drag force in axial direction
$F_f$: Floatation force on particle
$F_g$: Gravity force on particle
$x_i$: Spatial coordinate in the $i$-direction
$p$: Pressure
$D_{in}$: Diameters of inlet of long shroud
$D$: Diameter of swirling chamber
$d$: Diameter of inclusion particle
$H$: Height of swirling chamber
$F_c$: Centripetal force on particle
$a$: Radius of central vortex

Greek symbols

$\varepsilon$: Dissipation rate of kinetic energy
$\varepsilon_{in}$: Dissipation rate of kinetic energy at inlet
$\rho$: Density of fluid
$\rho_s$: Density of inclusion
$\mu$: Molecular viscosity of Fluid
$\mu_{eff}$: Effective viscosity of fluid
$\sigma_\varepsilon, \sigma_k, C_1, C_2, C_\mu$: Model constant for RNG and standard
$\omega$: Rotational velocity

## REFERENCES


1) Y. He and Y. Sahai: *Metall. Trans. B*, **18B** (1987), 81.
2) S. M. Lee, Y. S. Koo, T. Kang, I. R. Lee and Y. K. Shin: Proc. of The Sixth Int. Iron and Steel Cong., ISIJ, Tokyo, (1990).
3) P. K. Jha, S. K. Dash and S. Kumar: *ISIJ Int.*, **41** (2001), 1437.
4) J. Palafox-Ramos, J. De J. Barreto, S. López-Ramírez and R. D. Morales: *Ironmaking Steelmaking*, **28** (2001), 101.
5) C. M. Fan, R. J. Shie and W. S. Hwang: *Ironmaking Steelmaking*, **30** (2003), 341.
6) P. K. Jha, R. Ranjan, S. S. Mondal and S. K. Dash: *Int. J. Numerical Methods Heat Fluid Flow*, **13** (2003), 964.
7) V. Yakhot and S. A. Orszag: *J. Sci. Comput.*, **1** (1986), 3.
8) V. Yakhot and S. A. Orszag: *Phys. Rev. Lett.*, **57** (1986), 1722.
9) G. Th. Analytis: *Nucl. Eng. Des.*, **210** (2001), 177.
10) J. D. Ponser, C. R. Buchanan and D. Dunn-Rankin: *Energy Buildings*, **35** (2003), 515.
11) M. Yin, F. Shi and Z. Xu: *Int. J. Eng. Sci.*, **34** (1996), 243.
12) F. Z. Sierra-Espinosa, C. J. Bates and T. O'Doherty: *Comput. Fluids*, **29** (2000), 215.
13) B. W. Matthews, C. A. J. Fletcher and A. C. Patridge: *Appl. Math. Model.*, **22** (1998), 965.
14) J. L. Xia, G. Yadigaroglu, Y. S. Liu, J. Chmidli and B. L. Smith: *Int. J. Heat Mass Transfer*, **41** (1998), 1485.
15) G. Mompean: *Comput. Fluids*, **27** (1998), 847.
16) D. Mazumdar, G. Yamanogl and R. I. L. Guthrie: *Steel Res.*, **68** (1997), 293.
17) Y. Miki, S. Ogura and T. Fujii: *Kawasaki Steel Giho*, **35** (1996), 67.
18) Z. Zou, Q. Hou, S. Kuang and H. Li: Proc. 2nd Int. Conf. on Process Development in Iron and Steelmaking, Vol. 1, Metallurgical Research Institute AB, Luleå, (2004), 143.
(9) B. E. Launder and D. B. Spalding: *Comput. Methods Appl. Mech. Eng.*, **3** (1974), 269.
20) G. Solorio-Díaz, R. D. Morales, J. Palafax-Ramos, L. García-Demedices and A. Ramos-Bamderas: *ISIJ Int.*, **44** (2004), 1024.
21) J. Wu, H. Ma and M. Zhou: Introduction to Vorticity and Vortex Dynamics, High Education Press, Beijing, (1993), 194. (in Chinese)
22) A. K. Sinha and Y. Sahai: *ISIJ Int.*, **33** (1993), 556.